Revisiting γ-Alumina Surface Models through the Topotactic Transformation of Boehmite Surfaces

Thomas Pigeon, Céline Chizallet, Pascal Raybaud

Revisiting γ–alumina surface models through the topotactic transformation of boehmite surfaces

Thomas Pigeon,[1,2] Céline Chizallet,[1] P. Raybaud[1,2,*]

[1]IFP Energies Nouvelles, Rond-Point de l'Echangeur de Solaize,

BP 3, 69360 Solaize, France

[2]Univ Lyon, ENS de Lyon, CNRS UMR 5182, Laboratoire de Chimie,

F69342 Lyon, France

email : pascal.raybaud@ifpen.fr

Keywords : gamma-alumina, boehmite, topotactic transformation, density functional theory, surfaces, hydroxyls

Abstract

The rational understanding of γ–alumina (γ–Al_2O_3) supported catalysts requires an ever more improved atomic scale determination of the support's surface properties. By using density functional theory (DFT) calculations, we show how the structural and energetic surface properties of alumina crystallites intrinsically depend on its synthesis pathway. Considering the case study of the topotactic transformation of boehmite (γ–AlOOH) into γ–Al_2O_3 taking place during calcination, we propose a methodology to mimic this pathway by reconstructing relevant slabs of boehmite into γ–alumina slabs following 3 steps : dehydration, contraction/translation and Al migration into spinel or non-spinel sites. On the one hand, we confirm the reliability of some earlier $(1\,0\,0)$, $(1\,1\,0)$ and $(1\,1\,1)$ surface structures determined by standard bulk cleavage approach. Moreover, we find new γ–alumina surfaces harboring Brønsted acid sites (BAS) and Lewis acid sites (LAS) of specific local structure. More strikingly, we find that the basal $(1\,1\,0)_b$ surface of alumina inherited from the (010) basal surface of boehmite, exhibits a larger number of isolated μ_2-OH groups than the lateral $(1\,1\,0)_l$ surface. For the lateral $(1\,1\,0)_l$ orientation (respectively $(1\,1\,1)$ orientation), four (respectively three) thermodynamically competing surfaces are identified, including models earlier proposed. These results are induced by crystallites finite size and morphology effects during the topotactic transformation. Thanks to thorough comparative analysis of morphology and nature of BAS and LAS as a function of thermal treatment and water pressure for each surface, we identify coherent chemical families of surfaces across the main crystallographic orientations. These features open the door to a better differentiation of the reactivity of the basal alumina surfaces from the lateral ones.

1. Introduction

Alumina (Al_2O_3) is an inorganic oxide material existing as various polymorphs. Among these, the γ-polymorph is a chemically versatile transition alumina of high surface area exhibiting interesting Brønsted and Lewis acid-basic sites.[1, 2] Hence, the γ-alumina surface sites are very useful to promote its intrinsic acid-basic catalytic reactivity[2] as expected for biomass conversion,[3] or to allow the anchoring and dispersion of metallic active phases of various forms such as organometallic,[4] reduced,[5, 6] oxidized[7] or sulfided[8] ones. In the case of Mo sulfided active phase, γ-alumina is considered as the most widely used support, where the nature of the exposed surfaces was shown to influence key physico-chemical features[9-11] and catalytic activities[12] of the active phase. The location of inorganic dopant (phosphates) or metallic aggregates was also proposed to be surface sensitive.[13, 14] Hence, the continuous improvement of atomistic models of γ-alumina surfaces are necessary for the better control of the catalyst properties from the preparation steps[15] to the reaction conditions.[16]

In order to better characterize the local surface structure of these sites, numerous analytic experiments (IR, NMR, gravimetry)[17-23] and theoretical investigations[24-28] have been undertaken. The γ-polymorph is a transition alumina metastable within a specific temperature range below ~750°C. At higher temperatures, its crystallographic structure may evolve toward other polymorphs with lower surface area.[1] One of the most industrially used synthesis pathway of γ–alumina is the dehydration of the boehmite precursor (γ–AlOOH): following this thermal treatment process, the γ–alumina polymorph is formed at ~450°C.[1] The γ–AlOOH $\rightarrow$ γ–Al_2O_3 transformation is topotactic[1, 29-31] which means that simple relationships exists between the crystallographic axes of γ–AlOOH and those of γ–Al_2O_3. Such a topotactic transformation was also invoked for the synthesis of other materials such as iron oxides from their hydroxide precursor, e.g. α–FeOOH goethite and γ–FeOOH lepidocrite into α–Fe_2O_3

hematite and γ–Fe_2O_3 respectively.[32-34] Moreover, the shape of the individual platelets of both materials is conserved, as represented in **Figure 1a** for one hypothetical shape of boehmite platelet. Indeed, the shape of the boehmite and resulting alumina particles may depend on the boehmite synthesis conditions (such as pH or presence of organic surfactant).[35] For the present study, we will refer to this topotactic dehydration process. Obviously, other processes for the synthesis of alumina may be used such as oxidation of Al foil[36] or mechano-chemistry[37] which transformation process might differ from the topotactic one.

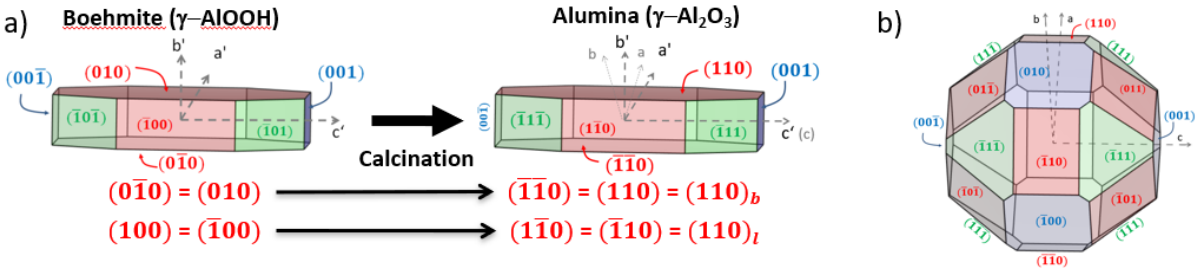

Figure 1: a) Topotactic transformation from a boehmite particle (left) to a γ-alumina particle (right). a', b' and c' correspond to boehmite *Cmcm* orientation axis while a, b and c correspond to conventional spinel directions used to express the alumina surface orientations. As the (**1 0 0**) and (**0 1 0**) boehmite surfaces are different, there is a priori no reason for them to be identical after dehydration, so the corresponding γ-alumina surfaces are named differently. b) Arbitrary spinel particle morphology with conventional spinel directions and corresponding Miller indices of the possible surface orientations.

Figure 1a also shows the correspondence between the $(h\ k\ l)$ facets of the starting boehmite material and those of alumina, according to the topotactic transformation. Since the earlier studies on the γ-alumina structure suggested that it may be similar to a spinel,[31, 38] the Miller indices for alumina facets reported in **Figure 1** are chosen according to this reference. The fact that alumina is not a perfectly defined crystalline material makes its structural determination

difficult, even if theoretical models have been proposed which improved our understanding of this material. Indeed, thanks to the possible applications of density functional theory (DFT) to γ–alumina supported catalytic systems of growing complexity,[16, 39, 40] the knowledge of this structure has been pushed forward, even if open questions remain.[41, 42]

Two different families were proposed for the γ-Al_2O_3 bulk structure: the defective spinel-like models in which only spinel positions are allowed [27, 43, 44] and non-spinel ones in which both spinel and non-spinel positions.[30, 45] The non-spinel model earlier proposed by Krokidis et al.[30] is based on an ideal mechanism of dehydration of boehmite and proposed to involve three key steps: dehydration of boehmite, translation/contraction of layers and Al migration from octahedral into tetrahedral sites. For the present study, we will use the latter, assuming that this topotactic process can be applied to build models for the $(h\ k\ l)$ surfaces of γ-alumina starting from surface models of boehmite, whereas the initial model of Krokidis et al. only considered the transformation of bulk boehmite into bulk γ-Al_2O_3.[30]

The true determination of these surfaces is critical for predicting the energetics of the particles (surface energy), which is a key descriptor of the reactivity and stability of the nano-materials. In particular, the surfaces bear the Brønsted or Lewis acid sites (BAS/LAS) involved in reactivity. BAS are constituted of aluminols (Al_x–OH), hydroxyl groups bonded to one or multiple surface LAS (aluminum ions) with flexible coordination numbers (4, 5, 6 when hydrated). Their reactivity depends on their local architecture depending itself on their location on the γ-alumina facets.[20] More recently, some edge models have also been proposed and revealed alternative accessible sites of alumina.[26] To simulate and investigate these surface sites by periodic density functional theory (DFT) approach, the most widely applied method in computational surface science is to cleave the bulk model of the material along the desired $(h\ k\ l)$ crystallographic orientations. This method was applied to the determination of γ–alumina surfaces from models of γ–alumina bulk by numerous previous studies.[24, 25, 27,

44, 46] However, this theoretical approach may be questioned when dealing with topotactic transformation such as the one depicted in **Figure 1a**, where crystallographic parentage affects not only the bulk structures of the starting material and final one, but also the shape and the surface structures.

As illustrated in **Figure 1**, the experimentally observed surfaces of γ–alumina particles are the (0 0 1), (1 1 0), (1 $\bar{1}$ 0), ($\bar{1}$ 1 1) and ($\bar{1}$ 1 $\bar{1}$) and their negative counterparts. The symmetry rules of the perfect spinel imply that all the surfaces having the same colors in **Figure 1b** are equivalent. If a topotactic transformation from common boehmite platelets (**Figure 1a**) is not used to synthesize γ–alumina and if the spinel symmetry holds, the equilibrium shape of the γ–alumina particles would be isotropic such as illustrated in **Figure 1b**. Such models have been proposed by previous studies[27, 42, 47] without considering that the synthesis pathway involved a topotactic transformation generating γ–alumina from its parent boehmite material. On the contrary, the alumina surfaces by Digne et al.[24, 25] were based on a bulk structure constructed on the basis of the topotactic transformation of the boehmite into alumina as suggested by Krokidis et al.[30] This method is illustrated by the top path of **Scheme 1** where the topotactic transformation is applied to 3D-periodic boundary conditions of the boehmite bulk cell (infinite material) and leads to the 3D-cell of bulk γ–alumina. Then, it is followed by the building of the slab model obtained by directly cleaving the alumina bulk in $(h\ k\ l)$ directions. In this case, no obvious distinction was made for the various possible surfaces belonging to one given $(h\ k\ l)$ family. In addition, it did not take into account the effect of finite size of the starting boehmite particles on the topotactic transformation mechanism. Considering the platelet morphology (**Figure 1a**) often invoked for boehmite nano-materials,[48] the (0 1 0) corresponds to the basal facet while (0 0 1), (1 0 0), and (1 0 1) surfaces correspond to lateral ones. The various (1 1 0) surfaces of γ–alumina are thus inherited from two parent boehmite surfaces which are not identical: the basal (0 1 0) and the lateral (1 0 0) surfaces. So,

it may be legitimately questioned why the two daughter alumina surfaces, called in what follows $(1\,1\,0)_l$ (label l stands for lateral) and $(1\,1\,0)_b$ (label b stands for basal), should become identical (**Figure 1a**) after a topotactic transformation (since the spinel symmetry of **Figure 1b** is not recovered).

In the present work, we investigate an alternative way of building such surface models (bottom path in **Scheme 1**). We will consider the initial boehmite slab models representing the most commonly exposed boehmite surface (**Figure 1a**) and we will build the alumina surfaces by applying the topotactic transformation to the slab models explicitly (being inspired by the Krokidis process,[30] but starting from boehmite slab models instead of boehmite bulk). The starting boehmite surfaces considered here will be the inequivalent $(0\,1\,0)$, $(0\,0\,1)$, $(1\,0\,0)$, and $(1\,0\,1)$ surfaces (**Figure 1a**). Their various possible hydration states were thoroughly investigated by DFT methods.[35, 49] Our work will analyze how the structural and energetic properties of the $(1\,1\,0)_b$, $(1\,1\,0)_l$, $(0\,0\,1)$, $(1\,1\,1)$ γ–alumina surfaces may differ according to the two approaches described in **Scheme 1**. In particular, we will quantitatively compare surface energies and nature of sites (BAS and LAS) exposed on each surface, as a function of relevant operating conditions (temperature, water partial pressure). For some of these orientations, we will propose surface models which differ from previous proposals, and which are likely to provide new understanding on surface acido-basicity of γ–alumina.

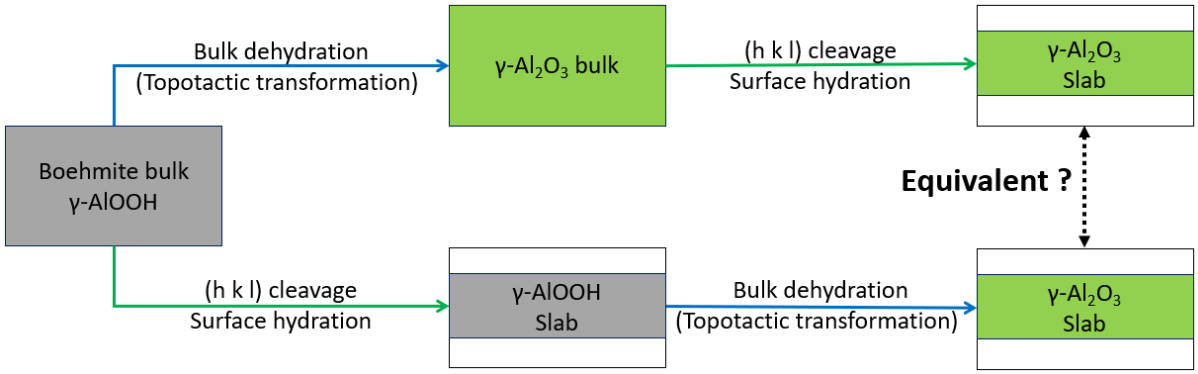

Scheme 1: Two ways of forming γ-Al_2O_3 surfaces involving the topotactic transformation from boehmite. Top path: topotactic transformation applied to the bulk, bottom path: topotactic transformation applied to the slabs. The topotactic transformation method is taken from Ref. [30]

2. Methods

The study has been conducted at the quantum level, on the basis of periodic Density Functional Theory (DFT) calculations. We used a plane-wave basis set with a 400 eV energy cutoff. We used the projector augmented wave (PAW) method for the pseudopotentials[50] as implemented in the Vienna Ab-initio Simulation Package (VASP).[51, 52] The exchange correlation functional used was the one proposed by Perdew, Burke and Ernzerhof (PBE)[53] with density dependent dispersion correction according to dDsC formalism.[54, 55] The energy of the reference water molecule has been computed at the same level of approximation (PBE-dDsC) in a cubic box of 10 Å at the gamma point. As expected, the use of dispersion corrections induced a systematic positive shift of surface energy values with respect to the previous work by Digne et al.[24, 25] A Gaussian smearing was used with a width of 0.05 eV and the convergence criterion for the SCF cycles was set at 10^{-7} eV. The non-spinel bulk model from ref.[30] had been fully relaxed with a 2x2x4 gamma point centered K-point grid and a 800 eV cutoff for the plane waves and a convergence criterion for the structure of 10^{-5} eV. The K point grid density for the slabs were identical to the bulk except in the direction in which the vacuum

was introduced where it was set to 1. To build the slabs in the $(1\ 1\ 1)$ orientation, the bulk structure has been firstly re-optimized in a reoriented cell containing 16 Al_2O_3 units with a 4x4x4 gamma point centered K-point grid. Then, as for all slab supercells, the relaxation of the atomic positions only has been performed with a 400 eV cutoff, before and after cleavage of the slabs. The convergence criterion for geometric relaxation was set to 0.01 eV $Å^{-1}$ on each atom of the bulk and slab models. The atomic coordinates of the most relevant atomic structures of γ–alumina surfaces are available from [56].

The thermodynamic diagrams were computed assuming that the only temperature dependent value was the water free energy, through its translational and rotational enthalpy and entropy. For selected systems, the vibrational components were taken into account both for gas phase water and hydroxylated slabs and showed a negligible influence on the computed surface dehydratation temperatures (**Supporting Information SI.1**). As we only computed free energy differences, this is equivalent to assuming that vibrational contributions balance out for the competing structures which would exhibit similar vibrational modes. Therefore, we compare the stability of the various structures on the basis on the electronic energy calculated at 0 K. The water adsorption free energy $\Delta_{Ads}G$ and the surface energy $\Gamma_{(khl)}$ were computed according to equations (1) and (2) respectively. In some cases, we also considered dehydration free energies which are computed by the same equations given $\Delta_{Ads}G = -\Delta_{dehydration}G$.

$$\Delta_{Ads}G\left(T, P_{H_2O}\right) = G_{Slab\,+\,n\,H_2O}(T) - G_{Slab\,+(n-1)H_2O}(T) - G_{H_2O}\left(T, P_{H_2O}\right) \approx E_{Slab+n\,H_2O} - E_{Slab+(n-1)H_2O} - G^{*}_{H_2O}\left(T, P_{H_2O}\right) \quad (1)$$

where $G^{*}_{H_2O} = E_{elec}(H_2O) + G^{rot}_{H_2O}\left(T, P_{H_2O}\right) + G^{trans}_{H_2O}(T, P_{H_2O})$

As aforementioned, in the $G^{*}_{H_2O}$ term, all vibrational contributions have been removed from G_{H_2O} to remain consistent with the same approximations made on the surface terms (E_{Slab} instead of G_{Slab}).

$$\Gamma_{(khl)} = \frac{1}{2A}\left(G_{Slab(N)+n\,H_2O}(T) - N\,G_{Bulk}(T) - n\,G_{H_2O}\left(T, P_{H_2O}\right)\right)$$

$$\approx \frac{1}{2A}\left(E_{Slab(N)+n\,H_2O} - N\,E_{Bulk} - n\,G^{*}_{H_2O}\left(T, P_{H_2O}\right)\right) \qquad (2)$$

where A stand for the surface area exposed on each side of the slabs, N the number of bulk units in the slab and n the number of water molecules adsorbed. $\Delta_{Ads}G$ stands for successive hydration energies.

The surface energies were computed according to equation (2), to determine bulk energy we computed it separately in a cell having the same orientations as the slab of interest. We assumed that vapor water is an ideal gas and thus included its rotational and translational free energies in gas phase. We must underline that all thermodynamic diagrams reported in this study are only valid for the domain where water can be considered in a gaseous state. For that reason, we recall in all (T, p) diagrams the liquid/vapor, solid/vapor and solid/liquid equilibria to identify the frontiers beyond which our thermodynamic model is not valid anymore. For the domain where water exists in liquid or solid state, this would require explicit or implicit simulation of water as undertaken in some dedicated studies with more sophisticated approaches beyond the scope of present work.[11, 57, 58]

3. Results

3.1 $(1\ 1\ 0)_b$ surface models

The first part of our work consists in applying the two construction methods explained previously (**Scheme 1**) to build the alumina surfaces. If we focus first on the $(1\ 1\ 0)$ family of surfaces exposed on alumina particle, the corresponding slabs can be obtained by a topotactic transformation of the $(0\ 1\ 0)$ slab of boehmite according to the mechanism proposed in the

bottom path of **Scheme 1**. As the (0 1 0) surface is generally the lowest energy surface exposed by boehmite particles, it is also the predominant one considered as the basal surfaces embracing the boehmite platelets.[35, 49] Since the boehmite to γ-alumina transformation is topotactic, the alumina surface and its corresponding slab created from the boehmite (0 1 0) surface (slab) is thus the (1 1 0) basal surface (slab), called $(1\ 1\ 0)_b$ in what follows (**Figure 1**).

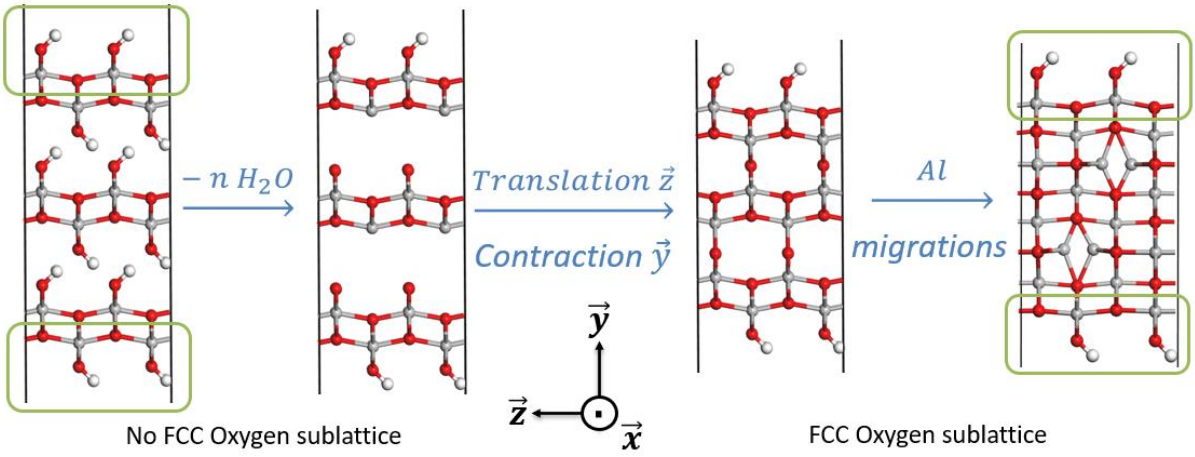

Figure 2: From left to right are represented the 4 first schematic transformation steps of the (**0 1 0**) slab adapted from ref. [30] : side view of the initial boehmite (**0 1 0**) slab; hypothetical boehmite (**0 1 0**) slab with interlayers dehydrated; (**0 1 0**) slab after translation and contraction process; final $(\mathbf{1\ 1\ 0})_\mathbf{b}$ slab of γ–alumina after Al diffusion. Color legend: red balls: oxygen, grey balls: aluminum, white balls: hydrogen. The green box highlights the surface structure before and after the first 4 steps of slab transformation. The axis system is taken from boehmite *Cmcm* representation.

The initial structure of the boehmite surface is presented in **Figure 2**. Notably, the four processes depicted in this Figure (dehydration, translation, contraction and al migration) are not necessarily consecutive in reality, some of these may take place jointly. A preliminary question is whether the dehydration of the surface occurs before or after the dehydration of the interlayers. As described in **Supporting information SI.2**, we found that the surface

dehydration energies are twice larger than the bulk dehydration energy. This dehydration of interlayer is further stabilized by the translation/contraction steps involved in the topotactic transformation of boehmite, before Al migrations occur in the bulk (**Figure 2**).[30] Hence, we will assume that during the first dehydration step, the bulk transforms first.

Following the internal slab reconstruction, we considered the possible migrations of Al atoms that can take place on the surface itself, which could lead to the surface reconstruction. Being inspired by the surface migration of Al atoms proposed by Wischert et al.[46], we investigated all the possible surface migrations and found that only two of them are possible to avoid too short Al-Al distances (**Figure 3**). For this reason, the two Al migrations represented by both blue arrows (respectively by green arrows) must occur simultaneously, while the green migrations must occur independently from the blue ones. The two types of migrations lead to two distinct surfaces induced by the coordination of sub-layer oxygen atoms (**Supporting Information SI.3**). Moreover, since the orientation of the bridging hydroxyls has an impact on the stability, eight surface configurations have optimized. Among all possible configurations detailed in **Supporting Information SI.3**, the most stable one is illustrated in **Figure 3b**.

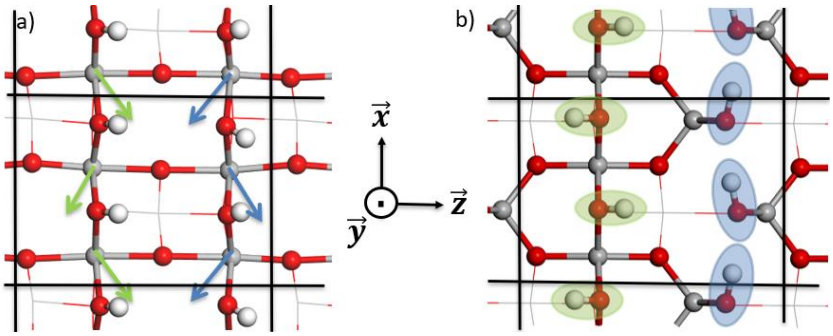

Figure 3:a) The two possible surface migrations of Al atoms from octahedral to tetrahedral sites on the $(\mathbf{1\ 1\ 0})_{\mathbf{b}}$ surface. Green arrows: migration 1, Blue arrows: migration 2. b) Most

stable structure after migration 2. Green and blue circles correspond to μ_2 and μ_1 hydroxyls respectively. Balls and sticks: surface layer; line: first sub-layer. Color legend: red balls: oxygen, grey balls: aluminum, white balls: hydrogen. The axis system corresponds to the boehmite *Cmcm* orientation so the normal to the surface is given by y.

At this stage, it is required to investigate the stability of this surface as a function of temperature and water pressure as it was proposed by Digne et al. for the original alumina (1 1 0) surface models.[24, 25] For that we systematically screened the removal of water molecules, and identified the thermodynamically most favorable hydrated states of this surface. The resulting surface energy curves (**Figure 4a**) show that this $(1\ 1\ 0)_b$ surface requires a treatment at high temperature (T> 850 K) even at low water pressure (< 10^{-6} bar) to be fully dehydrated. At water pressure higher than 10^{-2} bar, the surface remains hydrated (**Figure S5**). As it will be discussed later in detail, the fully hydrated surface exhibits an important number of isolated (non H-bond donor) bridging OH-μ_2-(Al_{VI},Al_{VI}). No other alumina surface model proposed so far, exhibits such amount of stable OH-μ_2 species directly reminiscent of the boehmite (0 1 0) surface. As we will discuss it in the next section, this behavior differs from the (1 1 0) surface model earlier proposed by Digne et al.[24, 25]

Thanks to the topotactic mechanism directly applied to γ–alumina bulk as proposed by Krokidis,[30] it is also possible to identify the (1 1 0) direction in the alumina bulk corresponding to the basal surface inherited from the (0 1 0) direction of the boehmite.[49] This protocol follows the top part of **Scheme 1**. There is only one possibility to construct a stoichiometric and symmetric slab (**Supporting information SI.4**). As it is not straightforward to calculate the surface energy of asymmetric slabs, we did not consider them. This is not the cleavage orientation that was formally chosen by Digne et al.,[24, 25] the later corresponding to the lateral (1 1 0) orientation, developed in the following section. After cleaving the bulk

along the direction corresponding to the basal $(1\ 1\ 0)$ orientation, the dehydrated surface is composed of two $Al_{IV\text{-}Ss}$ sites, two $O(Al_{IV\text{-}Td})(Al_{IV\text{-}Ss})$ and two $O(Al_{IV\text{-}Ss})(Al_{VI\text{-}Oh})_2$ (**Figure S6**). Notably, the first index after an Al atom is its coordination number and the second its VSEPR geometry (Oh: Octahedral, Td: Tetrahedral, Ss: Seesaw, SP: Square pyramidal). The thermodynamic diagrams (**Figure 4b and S7a**) reveals that this surface is more hydrated at low T (< 400 K) than the previous one, which leads to hydroxyl groups of μ_2-OH-($Al_{IV}Al_{VI}$), μ_1-OH-(Al_{VI}), μ_1-H_2O-(Al_{VI}) types at 18 OH.nm^{-2} (**Figure S6 e**). It becomes dehydrated at lower T whatever the pressure. However, the comparison of the evolution of surface energies of the two surface models obviously reveals the much greater stability of the $(1\ 1\ 0)_b$ surface built from the $(0\ 1\ 0)$ surface of boehmite over a wide range of realistic experimental conditions (**Figure 4c**). This trend remains true for higher water pressure as illustrated on the (P, T) thermodynamic diagrams where the solid/liquid/vapor equilibria of water are also represented **(Figures S7 b).** This shows that the $(1\ 1\ 0)_b$ model build by cleaving the bulk structure is never stabilized in the domain of vapor water.

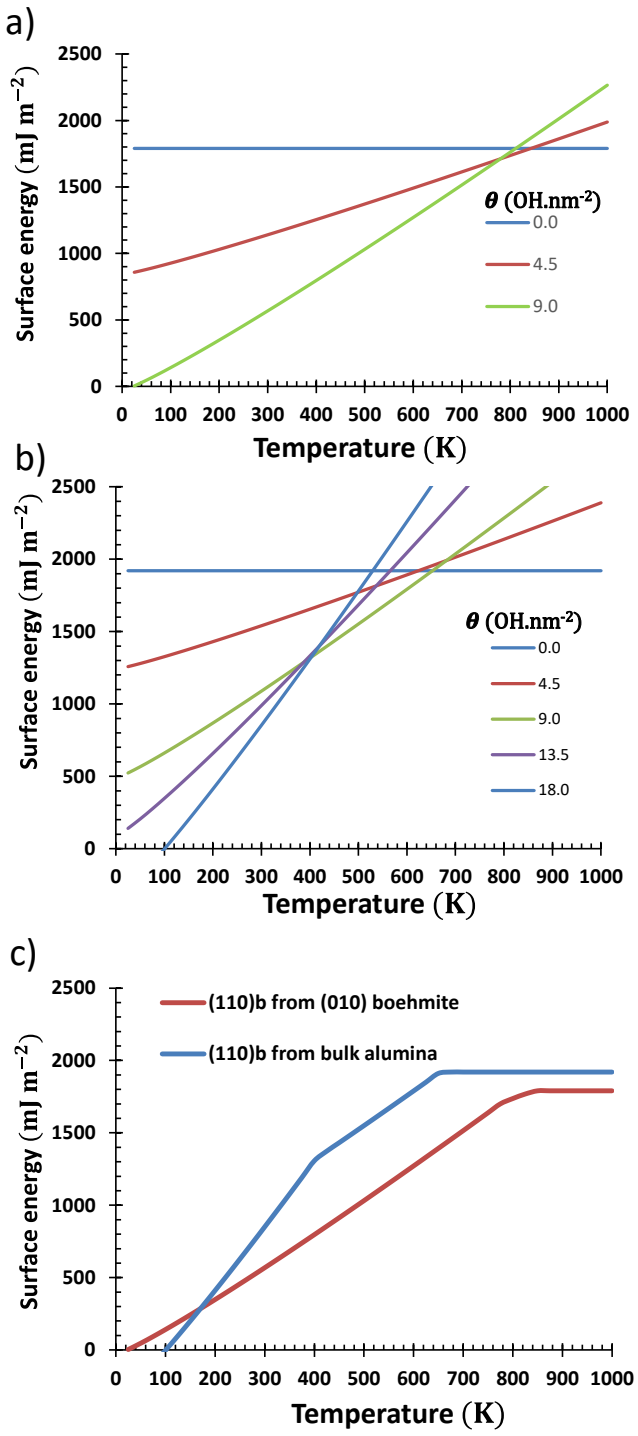

Figure 4: Surface energy curves as function of temperature at fixed water pressure (P_{H_2O} =10^{-6} bar) for the $(\mathbf{1\ 1\ 0})_\mathbf{b}$ surface. a) Model built from the $(\mathbf{0\ 1\ 0})$ boehmite slab, b) model built from the γ-alumina bulk cleavage, c) comparison of the minimum surface energy curve of each model. For other P_{H_2O}, the reader can refer the (P,T) thermodynamic diagrams reported in **Figure S7b**.

3.2 $(1\ 1\ 0)_l$ surface models

As shown in **Figure 1**, the fully hydrated $(1\ 0\ 0)$ boehmite surface[35, 49] leads to the genesis of a $(1\ 1\ 0)$ γ-alumina surface during the topotactic transformation. As the $(1\ 0\ 0)$ surface is a lateral facet of the boehmite particles, we will call the corresponding alumina surface as $(1\ 1\ 0)$ lateral, and label it as $(1\ 1\ 0)_l$. Following the mechanism described on the bottom path of **Scheme 1**, the dehydration of the boehmite slab is presented in **Figure 5**. As detailed in **Supporting information SI.5,** four different surface models can be obtained by this method, depending on the type of bulk and surface Al atoms migrations involved during the last step of the transformation. Unlike the $(1\ 1\ 0)_b$ surface, our analysis reveals that this approach leads to the same models as the approach going through bulk alumina (top path of **Scheme 1**) that we will describe in what follows.

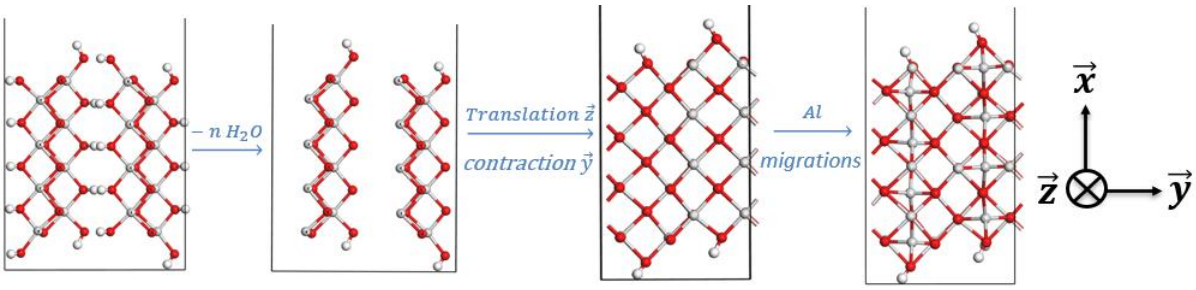

Figure 5: From left to right are represented the 4 first schematic transformation steps of the $(1\ 0\ 0)$ slab adapted from ref. [30] : side view of the initial boehmite $(1\ 0\ 0)$ slab; hypothetical boehmite $(1\ 0\ 0)$ slab with interlayers dehydrated; $(1\ 0\ 0)$ slab after translation and contraction process; final $(1\ 1\ 0)_l$ slab of γ–alumina after Al diffusion. Color legend: red balls: oxygen, grey balls: aluminum, white balls: hydrogen. The axis system is taken from boehmite *Cmcm* representation.

Indeed, building a surface model corresponding to the same orientation by cleaving the bulk γ–alumina model leads to considering four distinct slab models as illustrated in **Figure 6**. The slab thicknesses are adjusted so that the slabs are symmetric.

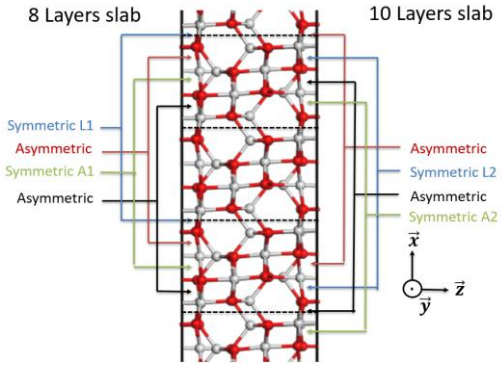

Figure 6: Periodic structure of bulk γ-Al_2O_3 non-spinel model. The structure was multiplied several times in the (**1 0 0**) boehmite direction (x axis) to illustrate the different possibilities to build symmetric slabs in this direction, representing the $(\mathbf{1\ 1\ 0})_l$ surface by cleavage of the γ-Al_2O_3 bulk structure. The axis system is taken from boehmite *Cmcm* representation. The names of the different symmetric slabs are given based on surface organization of Al atoms as explained in the text.

The previous DFT calculations on this family of (1 1 0) surfaces compared the energies of the dehydrated surfaces at 0 K to identify the most favorable termination.[24, 25] In the present work, we propose to go further by comparing hydrated surface models also. Actually these four models could be split in two main groups based on the nature of surface hydroxyls, directly related to the surface Al arrangement: two models labelled "L" for which the surface $Al_{IV\text{-}Ss}$ are aligned in the y direction (using boehmite's axes, see **Figure S8)**, and two models labelled "A" for which they are alternated. In addition, two Al distributions in subsurface may exist for each model type, labelled as Lx and Ax (x=1 and 2). In particular, the A1 surface corresponds to the one that has been studied by Digne et al.[24, 25] and Wischert et al.[46] We

built the full thermodynamic diagrams for the four models, accounting for their gradual hydration-dehydration structures. **Figure S10** shows that the Ax surfaces exhibit a continuous hydration/dehydration process (from 0 to 18 OH/nm^2). They stepwise adsorb or desorb water as a function of the thermal conditions and behaves like a sponge. By contrast, the Lx surfaces have a constant hydration state (12 OH/nm^2) over a large temperature domain and exhibit a discontinuous hydration/dehydration process, losing 9 OH/nm^2 at once above 800 K.

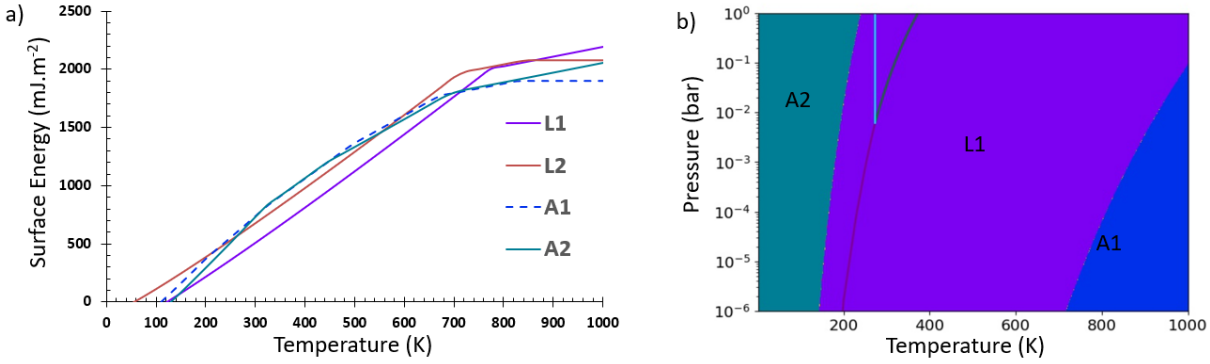

Figure 7: a) Evolution of the surface energy for the $(\mathbf{1\,1\,0})_l$ surfaces as a function of temperature at $P_{H_2O} = 10^{-6}$ bar. Each broken line corresponds to one given hydroxyl coverage minimizing the surface energy of the given surface (envelope of surface energy minima, see also detail in **Supporting Information SI.5)**. b) Stability domains of the various $(\mathbf{1\,1\,0})_l$ surfaces as a function of P_{H_2O} and Temperature. The 3 colored lines represent the solid/vapor, liquid/vapor and solid/liquid equilibria of water. The diagram is only valid on the right-hand side of lines where vapor exists.

Considering the envelope of surface energy minima (with minimization over the hydroxyl coverages) for each surface, **Figure 7** shows that all models are similarly stable in a rather large domain of reaction conditions. As previously shown by Digne et al.[24, 25] we confirm that the non-hydrated A1 surface (as cleaved) is the most stable at 0 K. When considering hydration effect, the A2 surface would be slightly preferred at very low T (<200

K). However, since this temperature is below the domain of vapor water, we cannot fully trust our thermodynamic model which would require the simulation of liquid water. The L1 surface appears as slightly more stable from 150 K to 700 K (at P_{H_2O}=10^{-6} bar), while the A1 (and to a less extent A2) surface becomes more stable above 700 K (including calcination conditions). However, given the DFT accuracy and assumptions on vibrational components of enthalpy and entropy, various surfaces are competing. This trend remains globally true whatever the pressure (**Figure 7b**), although the A1 surface is destabilized with respect to L1 at high pressure (> 0.1 bar).

3.3 (1 1 1) surface models

The topotactic transformation of boehmite (1 0 1) surfaces leads to the (1 1 1) alumina surfaces (**Figure 1**). The (1 0 1) and (1 0 $\bar{1}$) boehmite surfaces are equivalent but a priori, we cannot assume that this will be the same for the inherited γ–alumina surfaces. As for the surfaces previously studied, depending on the choices made for the Al migrations steps, different surface models can be obtained. The interesting part here is that depending on these choices either a (1 $\bar{1}$ 1) or a ($\bar{1}$ 1 1) surface will be built. These two surfaces are not equivalent in the non-spinel bulk model. We arbitrarily decided to name these different orientations: Dx for (1 $\bar{1}$ 1) and Px for ($\bar{1}$ 1 1). **Figure 8** illustrates the dehydration steps for the boehmite (1 0 1) slab leading to the D1 model. With this method we can build two models in direction D (which are symmetric if we start from a slab with four layers of Al atoms) and four models in direction P (which are symmetric if we start from a slab with five layers of Al atoms). We then compare these models to the ones obtained from the extended alumina bulk structure presented in **Figure 9** illustrating the construction of Dx model ((1 $\bar{1}$ 1) spinel orientation) and Px models (($\bar{1}$ 1 1) spinel orientation) slabs using bulk alumina structure as a basis.

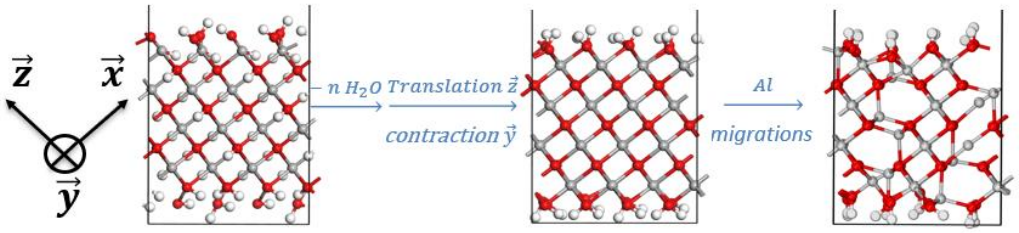

Figure 8: From left to right are represented the schematic transformation steps of the (**1 0 1**) boehmite slab into γ–alumina slab adapted from ref. [30]: side view of the initial boehmite (**1 0 1**) slab; hypothetical boehmite (**1 0 1**) slab with interlayers dehydrated and after translation and contraction process; one possible (**1 1 1**) slab of γ–alumina after Al diffusion. Color legend: red balls: oxygen, grey balls: aluminum, white balls: hydrogen. The axis system is taken from boehmite *Cmcm* representation.

Figure 9 shows that depending on the orientation, 2 families of slabs can be built. Here we recover the Dx and Px models. The Dx models found by dehydration of boehmite surface models can be easily recovered by cutting right above (or under for the bottom of the slab) the oxygen layer and adding one hydrogen atom on every oxygen atom. A representation of the two Dx slabs is given in **Figure S11**.

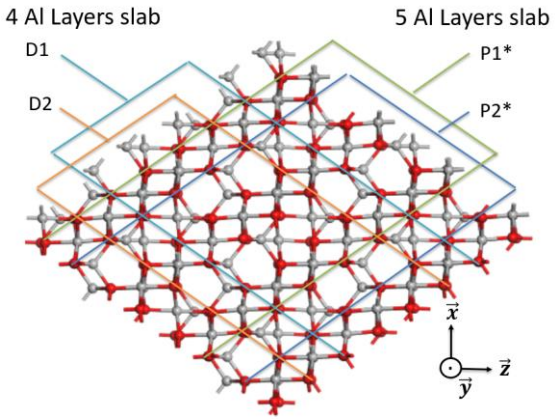

Figure 9: Periodic structure of bulk γ-Al_2O_3 non-spinel model. The structure was multiplied in the x and z boehmite direction to illustrate the different possibilities to build symmetric slabs

in these directions. The axis system is taken from boehmite *Cmcm* representation. The names of the different symmetric slabs are arbitrary. The * refers to the fact that doing a cleavage on those planes would lead some non-stoichiometric slabs.

The second family of (1 1 1) surface models is labelled as Px* (x=1 or 2) as shown in **Figure 9**. There are two ways of building a Px* slab induced by the possible migrations and locations of Al atoms, thus corresponding to 4 different P models, as illustrated in **Figure S11**. Overall, this leads us six different (1 1 1) slab models, which hydration-dehydration properties have been sampled systematically. The corresponding surface energy curves are provided in **Figure S12**, while **Figure 10** compares the relative stabilities of the hydrated surfaces by plotting the envelope of surface energy minima. As a consequence, the three most stable models are D1, D2 for the $(1\,\bar{1}\,1)$ orientation and P1_2 for the $(\bar{1}\,1\,1)$ which competing stability whatever P and T conditions. We recall that the D1 model is the same as the one previously proposed by Digne et al.[24, 25]

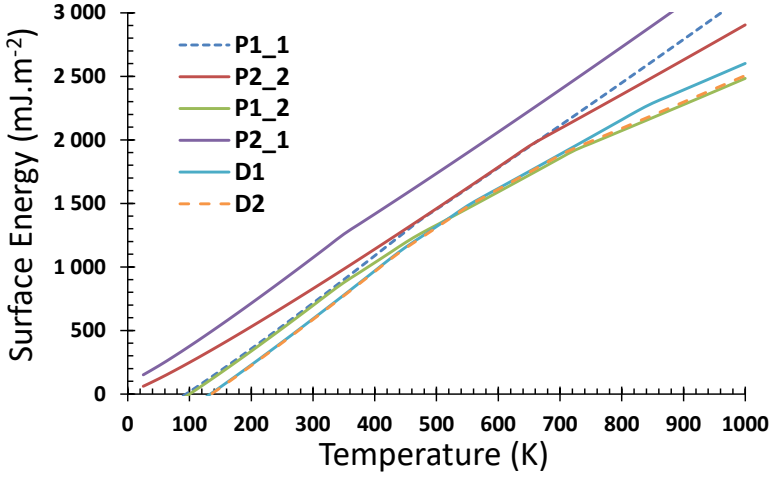

Figure 10: Lowest energy envelope of the different surface energies for the (**1 1 1**) lateral surfaces at $P_{H_2O} = 10^{-6}$ bar.

3.4 (**0 0 1**) surface models

As a preliminary remark, we underline that according to the spinel indexation used in previous works,[24, 25] the (0 0 1) surface was considered to be equivalent to the (0 1 0) and (1 0 0) surface. According to the revisited indexation explained in **Figure 1**, the (1 0 0) surface is called here (0 0 1) surface.

Due to the possible translation of the boehmite layers in the direction normal to the (0 0 1) surface, and depending on the layer stacking configuration of boehmite, the slab ends up with either a flat or a stepped surface (with stacking fault). **Figure 11** illustrates the case of a stepped (0 0 1) boehmite surface as a starting structure. If such a stepped boehmite surface is assumed, a flat alumina (0 0 1) surface (similar to the one proposed by Digne et al.[24, 25]) can be easily recovered according to the topotactic mechanism applied to the slab as shown in **Figure 11**. For sake of clarity, we decided to limit here our study to this mechanism leading to such a flat model of the alumina (0 0 1) surface. It is possible to consider more complex transformations starting from a flat (0 0 1) surface of boehmite and leading various alumina models either stepped or flat. Such an extension, beyond the scope of the present, could be interesting to be addressed in future investigations.

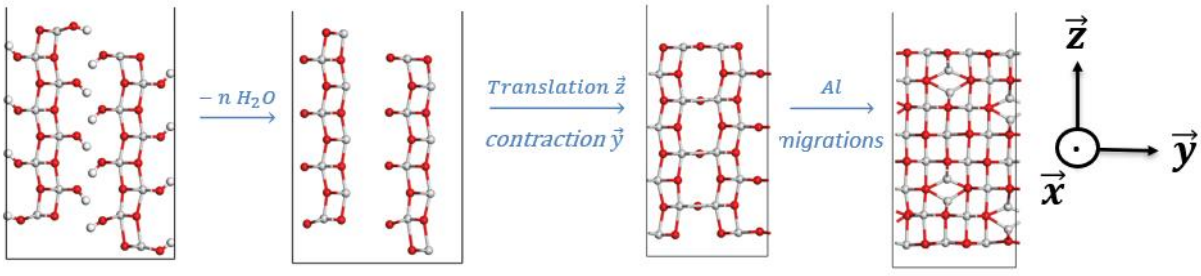

Figure 11: From left to right are represented the first 4 schematic transformation steps of the (**0 0 1**) slab adapted from ref. [30] : side view of the initial boehmite (**0 0 1**) slab exhibiting a stepped surface induced by stacking fault; hypothetical boehmite (**0 0 1**) slab with interlayers dehydrated; (**0 0 1**) slab after translation and contraction process; final (**0 0 1**) slab of

γ–alumina after Al diffusion. Color legend: red balls: oxygen, grey balls: aluminum, white balls: hydrogen. The axis system is taken from boehmite *Cmcm* representation.

In this case, the last Al migration step present different possibilities leading to four different models which cannot be all obtained by simply cleaving the γ–alumina bulk as described in **Supporting Information SI.7**. Hence, in this case, the two methods proposed in **Scheme 1** are not strictly equivalent. The most stable surface model between the four investigated is, however, exactly the same as the (1 0 0) surface one proposed by Digne et al.,[24, 25] with similar OH coverages stability domain as previously published.

4. Discussion

4.1 Impact of the topotactic transformation

Our previous results highlight one striking structural difference between the basal $(1\ 1\ 0)_b$ and lateral $(1\ 1\ 0)_l$ surfaces of alumina. Until now the available model,[25] considered to represent any kind of (1 1 0) facets, was the $(1\ 1\ 0)_l$A1 surface using the notation of the present work. Considering the two methods described in **Scheme 1** to generate γ-alumina surface models, we were able to build two distinct $(1\ 1\ 0)_b$ basal models. On top of being linked to its precursor, the model built through dehydration of a boehmite (0 1 0) slab is more stable than the one that could be proposed by direct cleavage of the alumina bulk.

Concerning the (1 0 0) boehmite surface which dehydrates into a 'lateral' (1 1 0) surface, we showed that the two methods described in **Scheme 1** are strictly equivalent. Pushing further the study of alternative $(1\ 1\ 0)_l$ terminations, we identified three alternative surface models that are completing the description of this $(1\ 1\ 0)_l$ surface: $(1\ 1\ 0)_l$A2, $(1\ 1\ 0)_l$L1 and $(1\ 1\ 0)_l$L2. The Lx models present some isolated μ_2-OH really similar to those observed on the $(1\ 1\ 0)_b$ model. The $(1\ 1\ 0)_l$A2 is really similar to the model labeled $(1\ 1\ 0)_l$A1 (corresponding to the

one earlier proposed[25]), while the $(1\,1\,0)_l$L2 (similar to $(1\,1\,0)_l$L1) differs from the alignment of the Al_{IV} sites.

Finally, for the $(1\,1\,1)$ and $(0\,0\,1)$ γ-alumina surfaces, the two methods are only partially equivalent, with differences due to slab's stoichiometry, symmetry and stacking conditions. We did not identify an improved model for the $(0\,0\,1)$ surface with respect to the one already existing though some further investigations could lead to alternative models (including stepped surfaces). Concerning the $(1\,1\,1)$ surface, dehydration of $(1\,0\,1)$ boehmite models allowed to recover the existing model,[25] labelled as $(1\,1\,1)$D1, and to propose two alternative models called $(1\,1\,1)$D2 and $(1\,1\,1)$P1_2.

From a methodological point of view, these findings illustrate how the theoretical mechanisms used for describing topotactic transformation should include the finite size character of the precursor boehmite nano-crystallites.

4.2 Surfaces stability and morphology as a function of experimental conditions

From an application point of view, it is interesting to compare first the energetics of the four more relevant surfaces constructed in the present study (**Figure 12**). Indeed, the surface energy may be considered as a descriptor for the intrinsic reactivity of the surfaces generated through topotactic transformation. While the $(0\,0\,1)$ surface exhibits the lowest surface energy over a large temperature range, it is not the predominant one and represents at most 20%, according to the rules of topotactic transformations.[29, 59] As previously discussed by Digne et al.[25], we thus confirm that the morphology of the γ–alumina particles obtained by topotactic transformation after calcination at ~800 K, is obviously metastable. It is interesting to notice first that even if the $(1\,1\,0)_b$ surface becomes slightly more stable than $(1\,1\,0)_l$ for temperature greater than 400 K (for a water pressure of 10^{-6} bar), the $(1\,1\,0)_b$ surface exhibits a higher surface energy than the $(0\,0\,1)$ surface. So, the newly obtained $(1\,1\,0)_b$ surface does

not strongly modify the stability ranking at 800 K. Moreover, since the $(1\,1\,1)$ and $(1\,1\,0)_l$ surfaces exhibit the higher surface energies, we may suspect that these facets are prone to be involved in the sintering process of the γ–alumina platelets.

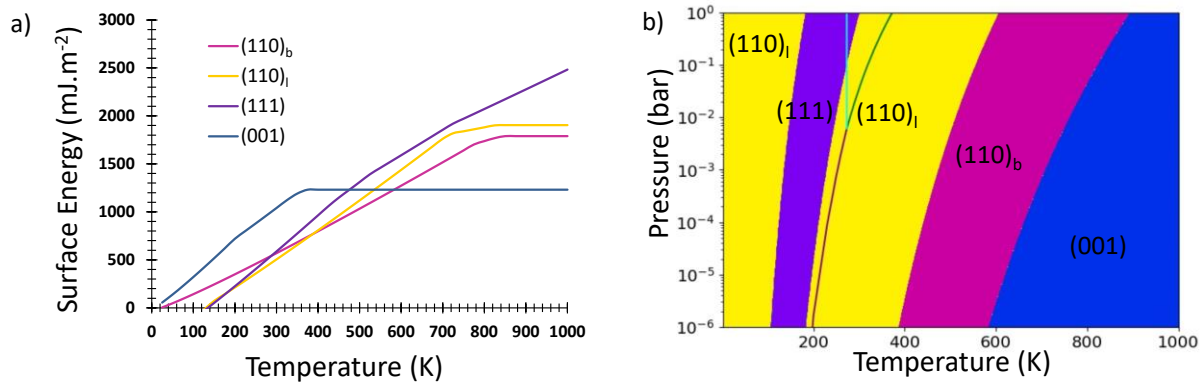

Figure 12. a) Lowest energy envelope of the surface energies for different relevant orientations at $P_{H_2O} = 10^{-6}$ bar. b) Stability domains of the various types of surfaces as a function of P_{H_2O} and Temperature. The 3 colored lines represent the solid/vapor, liquid/vapor and solid/liquid equilibria of water. The diagram is only valid on the right-hand side of the lines where vapor exists.

If we now consider a lower temperature regime (~300 K), **Figure 12** reveals that the surface energy ranking is completely different: the $(1\,1\,0)_b$ surface energy becomes now slightly higher than the $(1\,1\,0)_l$ surfaces. This effect is due to the energy gain of water adsorption on the $(1\,1\,0)_l$ and to a less extent to the $(1\,1\,1)$ surfaces which exhibit more undercoordinated Al sites than the $(0\,0\,1)$ surface (as discussed later). Hence, depending on the synthesis (T, P) conditions or whether a topotactic transformation is involved or not, the relative stability of facets is impacted which may thus modify the equilibrium morphology.

Interestingly, when increasing the water pressure, the stability domain of the $(0\,0\,1)$ and shrinks at the profit of the $(1\,1\,0)_b$, the $(1\,1\,0)_l$ or the $(1\,1\,1)$ surface depending on T and

pressure (**Figure 12 b**). This implies that the environmental conditions might impact the morphology and type of facets exposed by the γ–alumina particles due to the preferential dissociative adsorption of water on some facets.

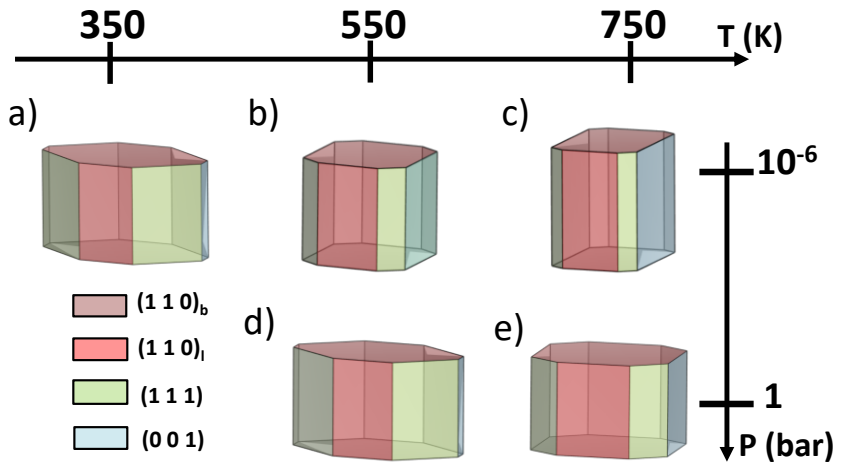

Figure 13. γ–alumina crystallite morphologies deduced from DFT surface energies (**Figure 12 a**) at three temperatures (350, 550 and 750 K), two water pressures ($P=10^{-6}$ and 1 bar) by using the γ–alumina surfaces and their energies after a topotactic transformation of boehmite. The numerical proportions of facets are reported in **Table 1**.

The morphology trend is quantified in **Figure 13** where the Gibbs-Curie-Wulff morphology [60, 61] was determined for three relevant temperatures (350, 550 and 750 K) and two water pressures considering two different assumptions. The first one assumes that a topotactic process leads to a parallelepiped like morphology are inherited from boehmite crystallite, i.e. exhibiting the $(1\ 1\ 0)_b$ facet (also inherited from $(0\ 1\ 0)$ boehmite) as a basal plane, all other facets being lateral $(1\ 1\ 0)_l$, $(0\ 0\ 1)$ and $(1\ 1\ 1)$ ones, normal to the basal one. Notably, for a strictly topotactic transformation, the equilibrium shape should be deduced from the surface energy of boehmite, and not that of γ-Al_2O_3. Using the DFT calculated surface energies of γ–alumina as defined in **Figure 12 a)**, the basal $(1\ 1\ 0)_b$ surface represents 32-36% whatever the (T, $P(H_2O)$) conditions (**Table 1)**. The lateral $(1\ 1\ 0)_l$ is also rather constant (16-

20%). By contrast, the relative proportions of the two other lateral facets are much more sensitive to the conditions. For the lower temperature (350 K) and/or higher water pressure (1 bar), the proportion of the most hydroxylated $(1\ 1\ 1)$ facets are predominant (~40%) at the detriment of the $(0\ 0\ 1)$ lateral facet (~5%). As the temperature increases and/or water pressure decreases, the surface energy of the $(0\ 0\ 1)$ is the one that increases the least, so that its proportion is enhanced, reaching ~37% for T=750 K and $P(H_2O)=10^{-6}$ bar. Such a proportion is compatible with the one earlier reported by experimental studies.[29]

	350 K	550 K		750 K	
Surface - Multiplicity		**10^{-6} bar**	**1 bar**	**10^{-6} bar**	**1 bar**
$(1\ 1\ 0)_b - 2$	36	36	36	32	37
$(0\ 0\ 1) - 2$	5	26	5	37	21
$(1\ 1\ 0)_l - 2$	17	20	19	19	20
$(1\ 1\ 1) - 4$	42	18	40	12	22

Table 1. Proportion (%) of each facet for the parallelipedic morphology as a function of temperature and water pressure (corresponding to **Figure 13**).

In **Supporting Information SI.8**, we also discuss different morphologies obtained by two different methods which are not based on topotactic transformation but rather on γ–alumina and spinel bulk equilibrium shape. For T=550 K or $P(H_2O)$=1 bar, it is observed that the shape is ovoid-like for γ–alumina bulk which is at variance with the one obtained for a pure spinel bulk (**Figure S14**) that leads to a more spherical shape at 550 K. Interestingly, parallelepipedic and ovoidal shapes have been observed experimentally by transmission electron microscopy (TEM)[26], which may imply that a purely defective spinel structure for γ–gamma polymorph must be ruled out as discussed in previous works.[26, 41, 45, 62]

As a corollary (valid for all morphologies), we observe that increasing the water pressure from 10^{-6} bar to 1 bar induces a morphology change similar as for a temperature decrease from 750 K to 550 K, which is interpreted as an effect induced by the evolution of surface hydration state.

Such morphology changes may also occur also during catalytic reactions involving water formation as a byproduct at a given temperature. At T~500-550 K corresponding to some biomass conversion or Fischer-Tropsch synthesis process, at low water pressure (low conversion), the (0 0 1) facet would exhibit 26% (**Table 1**). When water is produced in the course of the reaction at higher conversion, the (1 1 1) facet becomes thermodynamically favored (40%) while the (0 0 1) is destabilized (5%).

As discussed in the next section, the hydroxyl coverages and sites exposed by these facets are also significantly different, so their reactivity might change impacting either the overall catalyst activity or the support stability as reported by many experimental studies.[63-65]

4.3 Nature of the surface sites

Our work has also significant implications for the surface properties of γ–alumina prepared from boehmite precursor, following a topotactic transformation during the calcination process. We discuss in what follows how different BAS (OH groups) and LAS (exposed aluminum ions) can be identified on the different surface models. The various types of sites for the most relevant models are reported in **Table S6**, by choosing various sets of experimental conditions from low temperature close to mild thermal treatment such as drying conditions (400 K) to harsher thermal treatment such as calcination conditions (700-800 K). These conditions may also correspond to various reaction conditions applied during chemical processes using alumina supported catalysts.[3, 4, 7, 8, 66] The vapor pressures were also chosen from 10^{-2} to 10^{-6} bar to screen various possible water containing environment.

As expected, and already shown by previous studies, **Table S6** shows that the hydroxylation state (number and type of OH) and its thermal evolution clearly depend on the type of surfaces. The surfaces $(1\ 1\ 0)_l$A1, $(1\ 1\ 0)_l$A2, (1 1 1)D2, (1 1 1)P1_2 and to a lower extent (1 1 1)D1

exhibit a rather continuous decrease of the hydroxyl concentrations with temperature increase, whereas the $(1\ 1\ 0)_b$, $(1\ 1\ 0)_l$L1 and $(1\ 1\ 0)_l$L2 surfaces reveal a more discontinuous one and refrain the release of water till high treatment temperature. These continuous/discontinuous trends are also clearly illustrated in **Figures 14 b, e** and **h** where the (P, T) diagrams of OH coverages are plotted for the three relevant $(1\ 1\ 0)$ surfaces belonging to these 2 families. The discontinuous trend could not be found by previously published sets of $(1\ 1\ 0)$ models and it is intrinsically linked to the coordination number of OH groups and of the Al sites to which they are bonded. μ_2-OH (OH coordinated to two Al sites) and μ_1-OH groups bonded to Al_{IV} site are predominant on the surfaces $(1\ 1\ 0)_b$, $(1\ 1\ 0)_l$L1 and $(1\ 1\ 0)_l$L2, and are stable at higher temperature and/or lower vapor pressure with respect to other surface orientations. By contrast, μ_1-OH or μ_1-OH_2 bonded to Al_{VI} sites present on the $(1\ 1\ 0)_l$A1, $(1\ 1\ 0)_l$A2, $(1\ 1\ 1)$D2, and $(1\ 1\ 1)$D1 are removed at mild temperature. One small exception to this rule is the $(1\ 1\ 1)$P1_2 surface which exhibits μ_2- and μ_3-OH groups. However, since the hydroxyl concentration is very high (14.8 $OH.nm^{-2}$), this induces a destabilization of μ_2-OH groups which recombine with proton of μ_3-OH groups and leave the surface at mild temperature.

Among all the surface studied here, the family of $(1\ 1\ 1)$ surfaces is the one which keeps the highest concentration of BAS (from 7.3 to 9.8 $OH.nm^{-2}$) even for high temperature and/or low vapor pressure (**Figures S10)**. They exhibit a high number of μ_3-OH and μ_2-OH BAS which may explain their intrinsic stabilities. These surface hydroxyls might present a high Brønsted acidity, due to the great lability of proton attached to highly coordinated O atoms such as of the μ_3-OH-($Al_{VI}Al_{VI}Al_x$) on the $(1\ 1\ 1)$P1_2 surface. At high temperature, they also exhibit Lewis acidity borne by $Al_{V\text{-}SP}$ sites. Conversely, as it was already observed by Digne et al.[25], the $(0\ 0\ 1)$ surface loses OH groups at low temperature and gives raise to Lewis acidity borne by $Al_{V\text{-}SP}$ site. The family of $(1\ 1\ 0)$ surfaces (either lateral or basal), behaves intermediately and exhibits OH BAS with concentration of 3 to 6 OH nm^{-2} even at high temperature and low vapor

pressure. The departure of OH groups induces the formation of LAS, the nature of which depends whether it is located on a $(1\ 1\ 0)_l$ or $(1\ 1\ 0)_b$ surface, as discussed in what follows.

The comparison of the relevant local structures of the $(1\ 1\ 0)_b$ and $(1\ 1\ 0)_l$ models is illustrated in **Figure 14**.

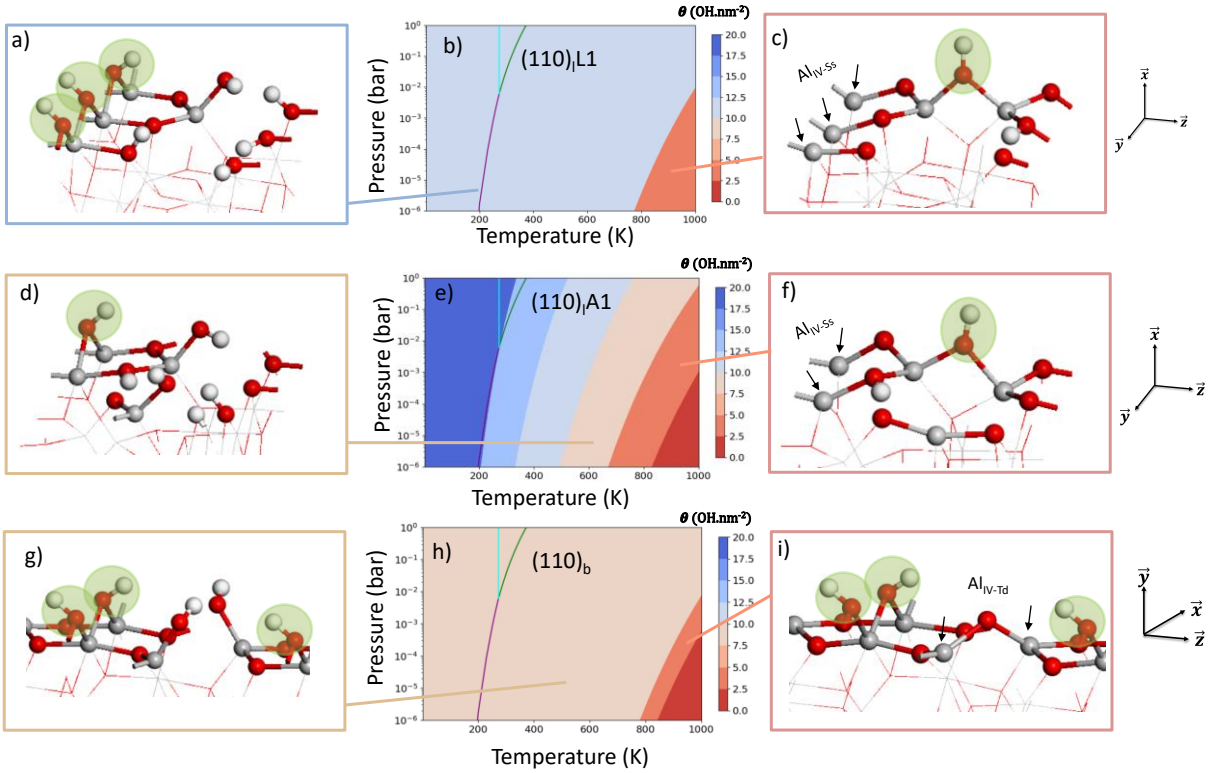

Figure 14. Three relevant **(1 1 0)** surface models at different hydroxyl coverages : a) $(\mathbf{1\ 1\ 0})_\mathbf{l}$L1 model at 12.0 OH.nm^{-2}; c) $(\mathbf{1\ 1\ 0})_\mathbf{l}$L1 model at 3.0 OH.nm^{-2} ; d) $(\mathbf{1\ 1\ 0})_\mathbf{l}$A1 model at 9.0 OH.nm^{-2}; f) $(\mathbf{1\ 1\ 0})_\mathbf{l}$A1 model at 3.0 OH.nm^{-2}; g) $(\mathbf{1\ 1\ 0})_\mathbf{b}$ model at 9.0 OH.nm^{-2}; i) $(\mathbf{1\ 1\ 0})_\mathbf{b}$ model at 4.5 OH.nm^{-2}. b) e) h) are plotting the corresponding (T, P) thermodynamic diagrams of hydroxyl coverages. The axis system is taken from boehmite *Cmcm* representation. Color legend: red balls: oxygen, grey balls: aluminum, white balls: hydrogen. μ_2-OH groups are circled in green, while $Al_{IV\text{-}Ss}$ are shown by black arrows. The 3 colored lines represent the solid/vapor, liquid/vapor and solid/liquid equilibria of water. The diagram is only valid on the right-hand side of the lines where vapor exists.

The $(1\ 1\ 0)_l$A1 model (**Figure 14 d and e**) is identical to the one proposed by Digne[24] and Wischert[46] while the $(1\ 1\ 0)_l$A2 is similar. The three other models $(1\ 1\ 0)_b$ (**Figures 14 g, i)** $(1\ 1\ 0)_l$L1 (**Figures 14 a, c)** and $(1\ 1\ 0)_l$L2 are different because they present significantly more OH-μ_2-Al_xAl_x BAS which are not H-bonded to another surface oxygen atom. This high number of isolated μ_2-OH groups found on these $(1\ 1\ 0)$ surfaces may corroborate observations made by ^{17}O NMR spectroscopy.[23] We also notice for the $(1\ 1\ 0)_b$ and $(1\ 1\ 0)_l$L1 surfaces a close proximity between isolated μ_2-OH groups which also corroborates other observations provided by ^1H–^1H DQ MAS NMR spectra.[67] The isolated μ_2-OH protons might be more accessible and more reactive than those involved in H-bonds. They might also play an important role for the Brønsted acidity of this material since the lability of protons will be enhanced with respect to H-bonded species.

Figures 14 a and d clearly show the main difference between the A and L models: the L models present 3 isolated OH-μ_2-(Al_{VI},Al_{VI}) per unit cell (circled in green) corresponding to 4.5 OH nm^{-2} while the A model exhibit only one OH-μ_2 per unit cell corresponding to 1.5 OH nm^{-2} (**Figures 14 d)**. The high concentration of OH-μ_2 (4.5 OH nm^{-2}) is also found on the $(110)_b$ surface model (**Figures 14 g and i)** over a wider range of (T, P) conditions. Their intrinsic stability explains the constancy of the hydroxyl coverage on a wide range of temperature for the L models while the A models desorb water more gradually.

Coming back to the Lewis acid sites, $Al_{IV\text{-}Td}$ are present on all $(1\ 1\ 0)$ surfaces and their interaction with the adsorbed water is the strongest. Interestingly, the leaving OH groups from $Al_{VI\text{-}Oh}$ present at the lateral surfaces generate LAS $Al_{V\text{-}SP}$ at mild temperature and $Al_{IV\text{-}Ss}$ (shown by black arrows in **Figure 14 c and f** at higher temperature. On the basal $(1\ 1\ 0)_b$ surface, the nature of LAS is less modified and remains of Al_{Td} type (black arrows in **Figure 14 i)** whatever the conditions which also indicates that this surface is intrinsically less flexible

and probably less reactive than the lateral ones due to the presence of strongly stable OH-μ_2-(Al_{VI},Al_{VI}) as illustrated in **Figure 14 i**.

Within the context of catalysis, these families of γ–alumina surfaces newly identified in this work, should provide alternative ways to tune the reactivity of the support with respect to organic or inorganic adjuvants. In particular, the different BAS and LAS sites located on the basal (101) and the lateral (101) surfaces should influence the interaction of the support with the metallic active phase and modulate the dispersion and reduction of metallic active phases. Such considerations are consistent with recent experimental works highlighting the impact of alumina facets on physico-chemical features of catalytic MoS_2 phases.[9, 10, 12]

5. Conclusion

By using periodic DFT calculations, we revisited the construction of γ–alumina surface models by two complementary methods based on the topotactic transformation of the boehmite precursor under thermal treatment process (such as calcination): the standard one, considering the cleavage of a bulk alumina model, and an alternative one, considering the finite size of boehmite crystallites. On the one hand, our work confirms the relevance of the three previous γ–alumina surface models[24, 25] related to the $(0\ 0\ 1)$, $(1\ 1\ 0)$ and $(1\ 1\ 1)$ crystallographic orientations obtained by the two methods. On the other hand, the alternative method provides three new relevant surface models: $(1\ 1\ 0)_b$, $(1\ 1\ 0)_l$L1 and $(1\ 1\ 1)$P1_2. These surface models, which are thermodynamically stable as a function of temperature and water pressure, exhibit some new populations in terms of types of hydroxyls with respect to previous models, that could be crucial to better understand γ-alumina surface properties.

In particular, we highlighted the key discrepancy between the basal and lateral $(1\ 1\ 0)$ surfaces. Until now a unique model (labelled $(1\ 1\ 0)_l$A1 in our notation) was representing both of them and corresponded to a lateral facet. Thanks to the alternative method,

the basal (1 1 0) surface is directly inherited from the (010) basal surface of its boehmite precursor and is highly stable according to its surface energy. Moreover, this $(1\ 1\ 0)_b$ model exhibits isolated surface μ_2-OH (free from H-bonds) that have seldom been found on the other surfaces.

Concerning the (1 0 0) boehmite surface which is transformed into a 'lateral' (1 1 0) γ-Al_2O_3 surface, we showed that the two methods are strictly equivalent. In both cases, we identified three alternative surface models that are completing the description of this $(1\ 1\ 0)_l$ surface: $(1\ 1\ 0)_l$A2, $(1\ 1\ 0)_l$L1 and $(1\ 1\ 0)_l$L2. The Lx models present some isolated μ_2-OH similar to those observed on the $(1\ 1\ 0)_b$ model, whereas the Ax models exhibit less isolated μ_2-OH.

For the (1 1 1) and (0 0 1) γ-alumina surfaces, the two methods are partially equivalent only, due to slab's stoichiometry and symmetry problems for the slab's construction using the bulk cleavage approach. We did not identify an improved model for the (0 0 1) surface with respect to the one previously proposed.[24, 25] However, we observe that the final model might be influenced by stacking fault withing the layers of boehmite which may be the subject of future investigations. Concerning the (1 1 1) γ-Al_2O_3 surface, the topotactic transformation (101) boehmite slabs allowed to recover the earlier proposed model, (1 1 1)D1[18,19] and to identify a relevant alternative model called (1 1 1)P1_2.

From a methodological point of view, our work demonstrated that the two applied methods for constructing the surfaces: cleavage of γ–alumina bulk vs. topotactic transformation of boehmite slabs are not equivalent. In the same spirit as the mechanism of Krokidis et al. for building non-spinel γ–alumina bulk,[30] the topotactic transformation applied to boehmite slabs implies dehydration, layers translation/contraction and Al migration processes leading to stable spinel or non-spinel positions in the inner slabs and at their surface. Moreover, since the topotactic transformation occurs on nano-crystallites of boehmite's precursor, finite size effects

induced by these crystallites directly influence the structural filiation of surfaces exposed by the resulting alumina. As a corollary, the present work demonstrates that the simple cleavage of spinel model of alumina bulk to build γ–alumina surface as sometimes proposed in the literature[27, 42, 47] is not appropriate to describe the surfaces of alumina when alumina is synthesized through a boehmite calcination process involving the topotactic transformation.

The morphology based on Gibbs-Curie-Wulff construction revealed how the proportion of each facet evolves as a function of (T, $P(H_2O)$) conditions and depending on the synthesis pathway: parallelepipedic and ovoidal shapes have been thus highlighted. In the case of a topotactic transformation, the proportion of the basal $(1\ 1\ 0)_b$ facet inherited from boehmite remains stable ~32-37% whatever the (T, $P(H_2O)$) conditions considered here. In all cases, among the lateral facets, the $(1\ 1\ 1)$ and $(1\ 1\ 0)$ facets are predominant at low temperature or at high water pressure, whereas the $(0\ 0\ 1)$ is favored at high temperature or low water pressure.

As a first perspective, we suggest that this methodology based on the structural filiation of the precursor slabs should be applied for any material (such as Fe_2O_3) synthesized through a topotactic transformation of a precursor material. This method is the only way to rigorously determine the structural and energetic features of the surfaces exposed by the final material inherited from the precursor one. As a second perspective, the identification of new families of γ–alumina surfaces should provide alternative ways to tune the reactivity of the support with respect to organic or inorganic adjuvants from the preparation steps to reaction conditions. Also, these surfaces will provide the opportunity to explore in more detail the nature of alumina edge sites located at the intersection of two neighboring facets, as it was recently initiated for the $(1\ 1\ 0)_l$ / $(0\ 0\ 1)$ edge.[26]

Acknowledgements

Calculations were performed using HPC resources (Jean Zay and Occigen) from GENCI-CINES (Grant A0020806134) and ENER 440 from IFP Energies nouvelles. This work is part of the "RatiOnAl Design for CATalysis" (ROAD4CAT) industrial chair, project IDEXLYON funded by the French National Research Agency (ANR-16-IDEX-0005) and the Commissariat-General for Investment (CGI) within the framework of Investissements d'Avenir program ("Investment for the future"). The authors thank the SYSPROD project and AXELERA Pôle de Compétitivité for financial support (PSMN Data Center).

REFERENCES

[1] P. Euzen, P. Raybaud, X. Krokidis, H. Toulhoat, J.-L.L. Loarer, J.-P. Jolivet, C. Froidefond, Handbook of Porous Solids, Wiley-VCH Verlag GmbH, Weinheim, 2002.
[2] G. Busca, Catal. Today 226 (2014) 2.
[3] K. Larmier, C. Chizallet, N. Cadran, S. Maury, J. Abboud, A.F. Lamic-Humblot, E. Marceau, H. Lauron-Pernot, ACS Catal. 5 (2015) 4423.
[4] C. Copéret, A. Comas-Vives, M.P. Conley, D.P. Estes, A. Fedorov, V. Mougel, H. Nagae, F. Núñez-Zarur, P.A. Zhizhko, Chem. Rev. 116 (2016) 323.
[5] M. Boudart, Catalysis by Supported Metals, in: D.D. Eley, H. Pines, P.B. Weisz (Eds.) Adv. Catal., Academic Press, 1969, pp. 153.
[6] A.T.F. Batista, W. Baaziz, A.-L. Taleb, J. Chaniot, M. Moreaud, C. Legens, A. Aguilar-Tapia, O. Proux, J.-L. Hazemann, F. Diehl, C. Chizallet, A.-S. Gay, O. Ersen, P. Raybaud, ACS Catal. 10 (2020) 4193.
[7] I.E. Wachs, Catal. Today 27 (1996) 437.
[8] H. Toulhoat, P. Raybaud, Catalysis by Transition Metal Sulfides. From molecular theory to industrial applications., Technip Edition, Paris (France), 2013.
[9] C. Bara, L. Plais, K. Larmier, E. Devers, M. Digne, A.F. Lamic-Humblot, G.D. Pirngruber, X. Carrier, J. Am. Chem. Soc. 137 (2015) 15915.
[10] R. Garcia de Castro, J. Bertrand, B. Rigaud, E. Devers, M. Digne, A.-F. Lamic-Humblot, G. Pirngruber, X. Carrier, Chem. Eur. J. 26 (2020) 14623.
[11] R. Reocreux, E. Girel, P. Clabaut, A. Tuel, M. Besson, A. Chaumonnot, A. Cabiac, P. Sautet, C. Michel, Nat. Commun. 10 (2019) 1.
[12] R. Garcia de Castro, E. Devers, M. Digne, A.-F. Lamic-Humblot, G.D. Pirngruber, X. Carrier, J. Catal. (2021).
[13] A. Hühn, D. Wisser, M. Corral Valero, T. Roy, M. Rivallan, L. Catita, A. Lesage, C. Michel, P. Raybaud, ACS Catal. (2021) 11278.
[14] C.H. Hu, C. Chizallet, C. Mager-Maury, M. Corral-Valero, P. Sautet, H. Toulhoat, P. Raybaud, J. Catal. 274 99.
[15] M.C. Valero, P. Raybaud, J. Catal. 391 (2020) 539.
[16] P. Raybaud, D. Costa, M.C. Valero, C. Arrouvel, M. Digne, P. Sautet, H. Toulhoat, J. Phys.: Condens. Matter 20 (2008) 64235.
[17] A.A. Tsyganenko, V.N. Filimonov, J. Mol. Struct. 19 (1973) 579.
[18] C. Morterra, G. Ghiotti, F. Bocuzzi, S. Coluccia, J. Catal. 51 (1978) 299.
[19] G. Busca, V. Lorenzelli, V.S. Escribano, R. Guidetti, J. Catal. 131 (1991) 167.
[20] H. Knözinger, P. Ratnasamy, Catal. Rev. Sci. Eng. 17 (1978) 31.

[21] M. Lagauche, K. Larmier, E. Jolimaitre, K. Barthelet, C. Chizallet, L. Favergeon, M. Pijolat, J. Phys. Chem. C 121 (2017) 16770.
[22] C.-H. Chen, E. Gaillard, F. Mentink-Vigier, K. Chen, Z. Gan, P. Gaveau, B. Rebière, R. Berthelot, P. Florian, C. Bonhomme, M.E. Smith, T.-X. Métro, B. Alonso, D. Laurencin, Inorg. Chem. 59 (2020) 13050.
[23] Q. Wang, W. Li, I. Hung, F. Mentink-Vigier, X. Wang, G. Qi, X. Wang, Z. Gan, J. Xu, F. Deng, Nat. Commun. 11 (2020) 3620.
[24] M. Digne, P. Sautet, P. Raybaud, P. Euzen, H. Toulhoat, J. Catal. 211 (2002) 1.
[25] M. Digne, P. Sautet, P. Raybaud, P. Euzen, H. Toulhoat, J. Catal. 226 (2004) 54.
[26] A.T.F. Batista, D. Wisser, T. Pigeon, D. Gajan, F. Diehl, M. Rivallan, L. Catita, A.S. Gay, A. Lesage, C. Chizallet, P. Raybaud, J. Catal. 378 (2019) 140.
[27] H.P. Pinto, R.M. Nieminen, S.D. Elliott, Phys. Rev. B 70 (2004) 125402
[28] R. Wischert, P. Laurent, C. Copéret, F. Delbecq, P. Sautet, J. Am. Chem. Soc. 134 (2012) 14430.
[29] P. Nortier, P. Fourre, A.M. Saad, O. Saur, J.C. Lavalley, Appl. Catal. 61 (1990) 141.
[30] X. Krokidis, P. Raybaud, A.E. Gobichon, B. Rebours, P. Euzen, H. Toulhoat, J. Phys. Chem. B 105 (2001) 5121.
[31] B.C. Lippens, J.H.d. Boer, Acta Crystallographica 17 (1964) 1312.
[32] G. González, A. Sagarzazu, R. Villalba, Mater. Res. Bull. 35 (2000) 2295.
[33] Y. Cudennec, A. Lecerf, Solid State Sci. 7 (2005) 520.
[34] J. Pedrosa, B.F.O. Costa, A. Portugal, L. Durães, Mater. Chem. Phys. 163 (2015) 88.
[35] D. Chiche, C. Chizallet, O. Durupthy, C. Channeac, R. Revel, P. Raybaud, J.P. Jolivet, Phys. Chem. Chem. Phys. 11 (2009) 11310.
[36] B. Ealet, M.H. Elyakhloufi, E. Gillet, M. Ricci, Thin Solid Films 250 (1994) 92.
[37] A.P. Amrute, Z. Łodziana, H. Schreyer, C. Weidenthaler, F. Schüth, Science 366 (2019) 485.
[38] K.P. Sinha, A.P.B. Sinha, J. Phys. Chem. 61 (1957) 758.
[39] C. Chizallet, P. Raybaud, Catal. Sci. Technol. 4 (2014) 2797.
[40] C. Chizallet, Top. Catal. (2021) https://doi.org/10.1007/s11244.
[41] M. Digne, P. Raybaud, P. Sautet, B. Rebours, H. Toulhoat, J. Phys. Chem. B 110 (2006) 20719.
[42] R. Prins, J. Catal. 392 (2020) 336.
[43] K.E. Sickafus, J.M. Wills, N.W. Grimes, J. Am. Ceram. Soc. 82 (1999) 3279.
[44] G. Gutiérrez, A. Taga, B. Johansson, Phys. Rev. B 65 (2001) 012101
[45] G. Paglia, A.L. Rohl, C.E. Buckley, J.D. Gale, Phys. Rev. B 71 (2005) 224115.
[46] R. Wischert, C. Copéret, F. Delbecq, P. Sautet, Angew. Chem. 123 (2011) 3260.
[47] A.R. Ferreira, M.J.F. Martins, E. Konstantinova, R.B. Capaz, W.F. Souza, S.S.X. Chiaro, A.A. Leitao, J. Solid State Chem. 184 (2011) 1105.
[48] D. Chiche, M. Digne, R. Revel, C. Chanéac, J.-P. Jolivet, J. Phys. Chem. C 112 (2008) 8524.
[49] P. Raybaud, M. Digne, R. Iftimie, W. Wellens, P. Euzen, H. Toulhoat, J. Catal. 201 (2001) 236.
[50] G. Kresse, J. Joubert, Phys. Rev. B 59 (1999).
[51] G. Kresse, J. Furthmüller, Comput. Mater. Sci. 6 (1996) 15.
[52] G. Kresse, J. Furthmüller, Phys. Rev. B 54 (1996) 11169.
[53] J.P. Perdew, K. Burke, M. Ernzerhof, Phys. Rev. Lett. 77 (1996) 3865.
[54] S.N. Steinmann, C. Corminboeuf, J. Chem. Theory Comput. 7 (2011) 3567.
[55] S.N. Steinmann, C. Corminboeuf, J. Chem. Phys. 134 (2011).
[56] T. Pigeon, C. Chizallet, P. Raybaud, Atomic structures of the gamma-alumina surfaces, NOMAD repository & archive (2021) https://dx.doi.org/10.17172/NOMAD/2021.11.10-1.
[57] B.F. Ngouana-Wakou, P. Cornette, M.C. Valero, D. Costa, P. Raybaud, J. Phys. Chem. C 121 (2017) 10351.
[58] J. Carrasco, A. Michaelides, M. Forster, S. Haq, R. Raval, A. Hodgson, Nat. Mater. 8 (2009) 427.
[59] J.P. Beaufils, Y. Barbaux, J. Chim. Phys. 78 (1981) 347.
[60] G. Wulff, Z. Kristallogr. 34 (1901) 449.
[61] M.P. Curie, Bull. Soc. Min. France 8 (1885) 145.
[62] C. Wolverton, K.C. Hass, Phys. Rev. B 63 (2000).

[63] J. Abi Aad, S. Casale, M. Michau, P. Courty, F. Diehl, E. Marceau, X. Carrier, ChemCatChem 9 (2017) 2186.
[64] M.W. Hahn, J.R. Copeland, A.H. van Pelt, C. Sievers, Chemsuschem 6 (2013) 2304.
[65] R.M. Ravenelle, J.R. Copeland, W.G. Kim, J.C. Crittenden, C. Sievers, ACS Catal. 1 (2011) 552.
[66] M. Boudart, Catalysis by Supported Metals, in, Elsevier, 1969, pp. 153.
[67] M. Taoufik, K.C. Szeto, N. Merle, I.D. Rosal, L. Maron, J. Trébosc, G. Tricot, R.M. Gauvin, L. Delevoye, Chem. Eur. J. 20 (2014) 4038.